International Journal of Humanoid Robotics
Vol. 13, No. 1 (2016) 1550039 (23 pages)

DOI: 10.1142/S0219843615500395

Improved Computation of the Humanoid Centroidal Dynamics and Application for Whole-Body Control

Patrick M. Wensing
Department of Mechanical Engineering,
Massachusetts Institute of Technology,
Cambridge, MA 02139, USA
pwensing@mit.edu

David E. Orin
Department of Electrical and Computer Engineering,
The Ohio State University, Columbus, OH 43210, USA
orin.1@osu.edu

Received 16 January 2015
Accepted 30 July 2015
Published 25 September 2015

The control of centroidal momentum has recently emerged as an important component of whole-body humanoid control, resulting in emergent upper-body motions and increased robustness to pushes when included in whole-body frameworks. Previous work has developed specialized computational algorithms for the centroidal momentum matrix (CMM) and its derivative, which relate rates of change in centroidal momentum to joint rates and accelerations of the humanoid. This paper instead shows that specialized algorithms are in fact not always required. Since the dynamics of the centroidal momentum are embedded in the joint-space dynamic equations of motion, the CMM and terms involving its derivative can be computed from the joint-space mass matrix and Coriolis terms. This new approach presents improvements in terms of its generality, compactness, and efficiency in comparison to previous specialized algorithms. The new computation method is then applied to perform whole-body control of a dynamic kicking motion, where the mass matrix and Coriolis terms are already required by the controller. This example motivates how centroidal momentum can be used as an aggregate descriptor of motion in order to ease whole-body motion authoring from a task-space perspective. It further demonstrates emergent upper-body motion from centroidal angular momentum (CAM) control that is shown to provide desirable regulation of the net yaw moment under the foot. Finally, a few perspectives are provided on the use of centroidal momentum control.

Keywords: Centroidal momentum; whole-body control; rigid-body dynamics.

1. Introduction

This paper derives new computationally-simple relationships between the structural components of the joint-space dynamic equations of motion for a humanoid and those of its centroidal momentum dynamics. The centroidal momentum[1,2] of a

rigid-body system consists of its net linear momentum as well as its net angular momentum about its center of mass (CoM). While the linear momentum has a well-known relationship with the velocity of the CoM, the centroidal angular momentum (CAM) has recently emerged as an important quantity within human and humanoid balance control.[3–7] Whole-body control strategies that employ centroidal momentum control can result in unauthored upper-body motions to maintain balance[1,4,6,7] and have been found to be more robust to disturbances than when inverse-dynamics-based control is applied.[8] Application of centroidal momentum planning has also been shown to simplify whole-body trajectory optimization,[9] by enabling collocation approaches to trade whole-body dynamics constraints within their formulation for significantly simpler ones on the evolution of centroidal momentum.

Although the net angular momentum of a system can be expressed about any point, angular momentum particularly about the CoM has been shown to be a privileged quantity in biomechanics studies of human walking.[3] Herr and Popovic[3] showed that their subjects had large non-zero angular momenta for individual bodies in their limbs, yet, the subjects' neuro-control systems coordinated significant inter-segmental momentum cancelations, regulating their CAM to near zero. This coordination strategy in human subjects has led roboticists to pursue its applicability as well. Originally, CAM was applied to automatically coordinate upper-body motions with the lower body by Kajita *et al.*[10] through resolved momentum control. Since then, CAM control has seen increasing applications for standing balance control on level,[4,11] uneven,[7] and non-stationary terrain.[5] While many locomotion control laws focus on point-mass simple models, other more sophisticated methods have begun to address angular momentum contributions for walking pattern generation[12,13] and have approximated these contributions for online applications.[14] Centroidal momentum control more specifically has also begun to be applied in locomotion,[6,15–17] and in the generation of rotational movements[18,19] for animated avatars.

Recently, Orin *et al.*[1,2] detailed the structure and properties of the centroidal momentum for a humanoid. They introduced the centroidal momentum matrix (CMM), which maps the generalized velocities of a humanoid to its centroidal momentum. A specialized computational algorithm for the CMM was originally presented, while others have introduced methods to compute the derivative of the CMM.[4,6] The net momentum of a rigid-body system has been studied from theoretical perspectives by others as well. Ostrowski and Burdick[20] studied the evolution of the net system momentum in the context of geometric mechanics. They showed how nonholonomic constraints which arise in wheeled vehicles can be exploited to shape otherwise conserved portions of the net system momentum. Wieber[21] later demonstrated the presence of the net Newton and Euler equations within the joint-space equations of motion for floating-base humanoid systems. While the development of Ostrowski and Burdick was largely coordinate free, Wieber's development used body-fixed coordinate systems for each rigid-body in the humanoid, and made a

portion of their observations much clearer for this class of systems. Featherstone[22] later showed how the net system momentum is included in the generalized momentum of a floating-base system.

With these insights, it is clear that the dynamics of the centroidal momentum (both linear and angular) are necessarily embedded in the whole-body dynamics of a humanoid. The usefulness of this observation to those working on centroidal momentum control, however, has eluded previous work in this area. As a main contribution of this paper, the work herein describes a general, compact, and efficient method to compute the CMM and a centroidal momentum bias force from knowledge of the joint-space mass matrix and Coriolis force respectively. The method is general in that it is compatible for application with any method that computes the structural components of the joint-space dynamic equations through Lagrangian, Kane's, or recursive Newton–Euler approaches alike. Our new methods to compute the CMM and its bias force are compact and efficient, providing simpler implementation and decreasing the computational overhead for the application of centroidal momentum control within a whole-body control framework. By providing these new connections to existing equations and algorithms in joint space, which many roboticists have access to, it is anticipated that the barrier to entry for centroidal momentum control will be decreased.

To motivate the use of this new computation strategy, we demonstrate the integration of centroidal momentum control within a whole-body control approach for a dynamic kicking motion. The application of centroidal momentum control is shown to provide emergent arm action and results in desirable properties on the ground reaction forces in comparison to when no CAM control is applied. The role of task prioritization in this application is finally described to assist future applications of whole-body momentum control.

The remainder of the paper is organized as follows. Section 2 provides a brief overview of centroidal momentum before the new computationally-simple relationships between the centroidal dynamics and the joint-space dynamic equations of motion are introduced in Sec. 3. Section 4 demonstrates the example of centroidal momentum control within a whole-body framework for a dynamic kicking motion, expanding upon our previous work.[7] Section 5 concludes with a summary.

2. Background

The centroidal momentum of a rigid-body system is a net momentum of all its bodies.[1,2] To review the background on centroidal momentum, standard notation[23] is adopted, including spatial (6D vector) notation. Spatial notation is used for compactness of presentation, while all results can be derived using conventional 3D vector notation. Given a floating-base humanoid system, its bodies are numbered 1 to N_B, with Body 1 selected to be the floating-base as shown in Fig. 1. The system is assumed to have n internal degrees of freedom (DoF) in addition to the 6-DoF floating-base joint.

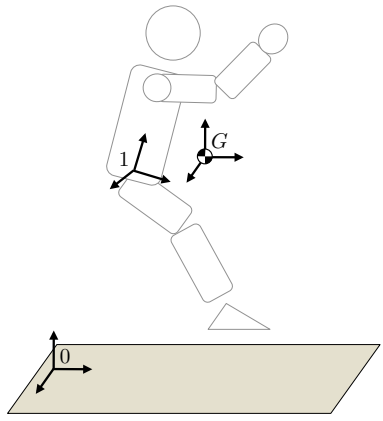

Fig. 1. Coordinate system definitions. The inertial coordinate system (ICS) 0 is earth fixed. The floating-base coordinate system 1 is rigidly attached to the torso in this example. The center of gravity (G) coordinate system is attached to the CoG with orientation parallel to the ICS.

The spatial momentum of Body i in this system, denoted $\mathbf{h}_i \in \mathbb{R}^6$, is comprised of its linear momentum $\boldsymbol{l}_i \in \mathbb{R}^3$ and its angular momentum $\boldsymbol{k}_i \in \mathbb{R}^3$ about a local coordinate origin.[a] The momentum of a body is related to its spatial velocity $\mathbf{v}_i \in \mathbb{R}^6$ through

$$\mathbf{h}_i = \begin{bmatrix} \boldsymbol{k}_i \\ \boldsymbol{l}_i \end{bmatrix} = \boldsymbol{I}_i \mathbf{v}_i, \tag{1}$$

$$= \boldsymbol{I}_i \begin{bmatrix} \boldsymbol{\omega}_i \\ \boldsymbol{v}_i \end{bmatrix}, \tag{2}$$

where $\boldsymbol{I}_i \in \mathbb{R}^{6\times 6}$ is a spatial inertia for Body i and takes the form

$$\boldsymbol{I}_i = \begin{bmatrix} \bar{\boldsymbol{I}}_i & m_i \boldsymbol{S}(\boldsymbol{c}_i) \\ m_i \boldsymbol{S}(\boldsymbol{c}_i)^T & m_i \mathbf{1} \end{bmatrix}. \tag{3}$$

Here $\boldsymbol{c}_i \in \mathbb{R}^3$ is the vector to the CoM for Body i, m_i its mass, and $\bar{\boldsymbol{I}}_i \in \mathbb{R}^{3\times 3}$ its standard Cartesian inertia tensor. $\boldsymbol{S}(\boldsymbol{p})$ provides the skew symmetric cross product matrix such that $\boldsymbol{S}(\boldsymbol{p})\boldsymbol{\omega} = \boldsymbol{p} \times \boldsymbol{\omega}$.

2.1. *Centroidal momentum*

The centroidal momentum of the system can be formed by adding up all the individual body momenta in the system. A coordinate frame G is placed at the CoM as shown in Fig. 1 to provide a common frame for all the body momenta. The centroidal

[a] As a standard practice, it is assumed that all quantities for Body i are given with respect to its local coordinate frame. A preceding superscript is used to indicate otherwise. For example, ${}^0\boldsymbol{p}_1$ gives the position of Body 1 in Body 0 (ICS) coordinates. See work by Featherstone and Orin[23] for further detail.

momentum can then be formed as

$$\mathbf{h}_G = \sum_{i=1}^{N_B} {}^i\boldsymbol{X}_G^{\,T}\mathbf{h}_i, \tag{4}$$

where the matrix ${}^i\boldsymbol{X}_G^{\,T} \in \mathbb{R}^{6\times 6}$ provides a spatial momentum transformation from Body i to the CoM frame. These transformations account for the different orientations of each link as well as their positional offsets from the CoM (G)

$${}^i\boldsymbol{X}_G^{\,T} = \begin{bmatrix} {}^G\boldsymbol{R}_i & {}^G\boldsymbol{R}_i\boldsymbol{S}({}^i\boldsymbol{p}_G)^T \\ \mathbf{0} & {}^G\boldsymbol{R}_i \end{bmatrix}. \tag{5}$$

By selecting the orientation of Frame G to be parallel to the ICS, the rotation matrix ${}^G\boldsymbol{R}_i \in SO(3)$ is equal to ${}^0\boldsymbol{R}_i \in SO(3)$.

2.2. *Centroidal momentum matrix*

The CMM $\boldsymbol{A}_G \in \mathbb{R}^{6\times(n+6)}$ of a floating-base system[1] linearly relates its generalized velocities $\dot{\boldsymbol{q}} \in \mathbb{R}^{n+6}$ to its centroidal momentum $\mathbf{h}_G$

$$\mathbf{h}_G = \boldsymbol{A}_G(\boldsymbol{q})\dot{\boldsymbol{q}}. \tag{6}$$

As is customary in robot dynamics, the generalized velocity is assumed to be composed of the individual joint velocities $\dot{\boldsymbol{q}}_i$

$$\dot{\boldsymbol{q}} = [\dot{\boldsymbol{q}}_1^{\,T} \cdots \dot{\boldsymbol{q}}_{N_B}^{\,T}]^T, \tag{7}$$

where $\dot{\boldsymbol{q}}_1 \in \mathbb{R}^6$ in particular provides a generalized velocity for the floating-base body through a relationship of the form[23,24]

$$\mathbf{v}_1 = \boldsymbol{\Phi}_1(\boldsymbol{q}_1)\dot{\boldsymbol{q}}_1. \tag{8}$$

The joint matrix $\boldsymbol{\Phi}(\boldsymbol{q}_1) \in \mathbb{R}^{6\times 6}$ can be defined to accommodate Euler angle rates or other representations of angular velocity within $\dot{\boldsymbol{q}}_1$.[23] As an example, $\dot{\boldsymbol{q}}_1$ could consist of the angular and linear velocity of the floating-base body in the ICS $\dot{\boldsymbol{q}}_1 = [{}^0\boldsymbol{\omega}_1^{\,T}\ {}^0\boldsymbol{v}_1^{\,T}]^T$, which provides $\boldsymbol{\Phi}_1$ through

$$\mathbf{v}_1 = \begin{bmatrix} \boldsymbol{\omega}_1 \\ \boldsymbol{v}_1 \end{bmatrix} = \underbrace{\begin{bmatrix} {}^1\boldsymbol{R}_0 & \mathbf{0} \\ \mathbf{0} & {}^1\boldsymbol{R}_0 \end{bmatrix}}_{\boldsymbol{\Phi}_1} \begin{bmatrix} {}^0\boldsymbol{\omega}_1 \\ {}^0\dot{\boldsymbol{p}}_1 \end{bmatrix}. \tag{9}$$

Through its proper use, $\boldsymbol{\Phi}_1$ is flexible to describe any selection of generalized velocity for the floating-base. However, most commonly for roboticists, the transformation $\boldsymbol{\Phi}_1$ is block diagonal as above, with the upper-left block accounting for the representation of angular velocity, and the lower-right block optionally providing a coordinate change for the linear velocity. This generality represents an improvement over previous methods for the centroidal dynamics that were presented assuming a single convention for the floating-base kinematics. It is important to note that a

choice of $\dot{\boldsymbol{q}}_1$ to include $\boldsymbol{\omega}_1$ and $\boldsymbol{v}_1$ directly is also valid, which would provide $\boldsymbol{\Phi}_1$ as the identity matrix.

Although (6) can be very useful on its own, the second-order *Centroidal Dynamics* are often required for dynamic whole-body controllers. Differentiation of (6) provides

$$\dot{\mathbf{h}}_G = \boldsymbol{A}_G \ddot{\boldsymbol{q}} + \dot{\boldsymbol{A}}_G \dot{\boldsymbol{q}}. \tag{10}$$

These centroidal dynamics are linked to the external forces on the system, as Newton's and Euler's laws require that $\dot{\mathbf{h}}_G$ be equal to the net external wrench $\mathbf{f}_G$ (force and moment about G) on the humanoid

$$\mathbf{f}_G = \dot{\mathbf{h}}_G = \boldsymbol{A}_G \ddot{\boldsymbol{q}} + \dot{\boldsymbol{A}}_G \dot{\boldsymbol{q}}. \tag{11}$$

$\mathbf{f}_G$ is usually comprised of the gravity force along with any ground reaction forces expressed at G.

Previous authors have developed special algorithms to compute the structural components of the centroidal dynamics. Orin *et al.*[1] provide an efficient $O(n)$ algorithm specialized to compute $\boldsymbol{A}_G$, while $O(n^2)$ methods to compute $\dot{\boldsymbol{A}}_G$ are given by Macchietto *et al.*[4] and in the errata to the paper by de Lasa *et al.*[6] Finite difference methods to compute $\dot{\boldsymbol{A}}_G$ provide an alternative method for computation which is $O(n)$ but more susceptible to finite precision numeric issues. Regardless of how they are computed, obtaining $\boldsymbol{A}_G$ and $\dot{\boldsymbol{A}}_G \dot{\boldsymbol{q}}$ to describe $\dot{\mathbf{h}}_G$ through (11) is the important first step towards selecting joint accelerations that provide angular momentum regulation in many centroidal momentum controllers.

3. Centroidal Dynamics Within the Joint-Space Equations of Motion

The specialized computational algorithms developed previously have enabled initial applications of centroidal momentum control. However, this section shows that no specialized algorithms are generally necessary. Instead, the mass matrix $\boldsymbol{H}$ and the Coriolis term $\boldsymbol{C}\dot{\boldsymbol{q}}$ from the joint-space dynamic equations of motion can be used to compute the centroidal dynamics quantities $\boldsymbol{A}_G$ and $\dot{\boldsymbol{A}}_G \dot{\boldsymbol{q}}$. This new computational approach has improved compactness and efficiency in comparison to previous methods, and thus has great potential to simplify future applications of centroidal momentum control where these structural components of the joint-space dynamic equations of motion are readily available.

To make the connection between these quantities, consider the joint-space dynamic equations of motion in a fully-actuated form but with no other external forces (no ground reaction forces)

$$\boldsymbol{H}(\boldsymbol{q})\ddot{\boldsymbol{q}} + \boldsymbol{C}(\boldsymbol{q}, \dot{\boldsymbol{q}})\dot{\boldsymbol{q}} + \boldsymbol{G}(\boldsymbol{q}) = \boldsymbol{\tau}. \tag{12}$$

$\boldsymbol{H} \in \mathbb{R}^{(n+6)\times(n+6)}$, $\boldsymbol{C}\dot{\boldsymbol{q}} \in \mathbb{R}^{n+6}$, $\boldsymbol{G} \in \mathbb{R}^{n+6}$, and $\boldsymbol{\tau} \in \mathbb{R}^{n+6}$ are the familiar mass matrix, velocity product term, gravitational term, and generalized force vector respectively.[23] Computation of the mass matrix $\boldsymbol{H}$ is required for any dynamic

whole-body control strategy and can be computed with the composite-rigid-body algorithm (CRBA), while $\boldsymbol{C}\,\dot{\boldsymbol{q}}$, $\boldsymbol{G}$, or their sum can be computed through recursive-Newton–Euler (RNEA) inverse dynamics approaches. Other symbolic techniques based on Lagrangian or Kane's methods are equally valid to compute the components of (12) for the purposes considered here. This generality represents an improvement over previous algorithms which have relied on particular conventions for the representation of the system dynamics.

The dynamic equations (12) can be partitioned into their floating-base and actuated components

$$\begin{bmatrix} \boldsymbol{H}_{11} & \boldsymbol{H}_{1*} \\ \boldsymbol{H}_{*1} & \boldsymbol{H}_{**} \end{bmatrix} \begin{bmatrix} \ddot{\boldsymbol{q}}_1 \\ \ddot{\boldsymbol{q}}_* \end{bmatrix} + \begin{bmatrix} \boldsymbol{C}_1\,\dot{\boldsymbol{q}} + \boldsymbol{G}_1 \\ \boldsymbol{C}_*\,\dot{\boldsymbol{q}} + \boldsymbol{G}_* \end{bmatrix} = \begin{bmatrix} \boldsymbol{\tau}_1 \\ \boldsymbol{\tau}_* \end{bmatrix}, \tag{13}$$

where $\boldsymbol{\tau}_1 \in \mathbb{R}^6$, $\boldsymbol{\tau}_* \in \mathbb{R}^n$, and associated definitions follow similarly. Although the floating-base is assumed actuated in this development, an unactuated floating-base would provide $\boldsymbol{\tau}_1 = \boldsymbol{0}$.

Given the joint matrix $\boldsymbol{\Phi}_1$ provided by the floating-base kinematics, virtual work dictates that the generalized force $\boldsymbol{\tau}_1$ is related to the wrench on the floating-base $\mathbf{f}_1 \in \mathbb{R}^6$ through[24]

$$\boldsymbol{\Phi}_1^{\,T}\,\mathbf{f}_1 = \boldsymbol{\tau}_1. \tag{14}$$

3.1. *Extraction of the centroidal dynamics*

Let us assume for the purposes of development, that the floating-base remains actuated and consider the dynamic equations in the absence of gravity ($\boldsymbol{G} = \boldsymbol{0}$). Under this assumption, the force on the actuated floating-base represents the only external force on the system. Defining $\boldsymbol{U}_1 = [\boldsymbol{1}_{6\times 6}\ \boldsymbol{0}_{6\times n}]$, it follows that

$$\boldsymbol{U}_1(\boldsymbol{H}\,\ddot{\boldsymbol{q}} + \boldsymbol{C}\dot{\boldsymbol{q}}) = \boldsymbol{\tau}_1 = \boldsymbol{\Phi}_1^{\,T}\mathbf{f}_1. \tag{15}$$

Further defining $\boldsymbol{\Psi}_1 = \boldsymbol{\Phi}_1^{-1}$, the net external wrench in Frame 1 is

$$\boldsymbol{\Psi}_1^{\,T}\,\boldsymbol{U}_1(\boldsymbol{H}\,\ddot{\boldsymbol{q}} + \boldsymbol{C}\dot{\boldsymbol{q}}) = \mathbf{f}_1. \tag{16}$$

The spatial transform ${}^1\boldsymbol{X}_G^{\,T}$ can be used to instead examine the net external wrench in Frame G, $\mathbf{f}_G$, which is equal to $\dot{\mathbf{h}}_G$ through (11)

$$\begin{aligned} \mathbf{f}_G &= {}^i\boldsymbol{X}_G^{\,T}\,\mathbf{f}_1, & (17)\\ &= {}^i\boldsymbol{X}_G^{\,T}\,\boldsymbol{\Psi}_1^{\,T}\,\boldsymbol{U}_1(\boldsymbol{H}\,\ddot{\boldsymbol{q}} + \boldsymbol{C}\dot{\boldsymbol{q}}), & (18)\\ &= \boldsymbol{A}_G\,\ddot{\boldsymbol{q}} + \ \dot{\boldsymbol{A}}_G\,\dot{\boldsymbol{q}}. & (19) \end{aligned}$$

Since this relationship must be true for any choice of $\ddot{\boldsymbol{q}}$, it follows that the CMM and the centroidal momentum bias force can be constructed from components of the dynamic equations of motion.

$$\boxed{\boldsymbol{A}_G = {}^1\boldsymbol{X}_G^T\ \boldsymbol{\Psi}_1^T\,\boldsymbol{U}_1\,\boldsymbol{H}} \tag{20}$$

$$\boxed{\dot{\boldsymbol{A}}_G\,\dot{\boldsymbol{q}} = {}^1\boldsymbol{X}_G^T\ \boldsymbol{\Psi}_1^T\,\boldsymbol{U}_1\,\boldsymbol{C}\,\dot{\boldsymbol{q}}} \tag{21}$$

That is, the CMM $\boldsymbol{A}_G$ and bias $\dot{\boldsymbol{A}}_G\,\dot{\boldsymbol{q}}$ can be computed from the mass matrix $\boldsymbol{H}$ and the Coriolis term $\boldsymbol{C}\,\dot{\boldsymbol{q}}$ through a set of kinematic transformations. Given that many applications of whole-body control require the computation of the mass matrix $\boldsymbol{H}$ and Coriolis term $\boldsymbol{C}\,\dot{\boldsymbol{q}}$, this represents little additional overhead in order to obtain $\boldsymbol{A}_G$ and $\dot{\boldsymbol{A}}_G\,\dot{\boldsymbol{q}}$ for the centroidal dynamics.

In order to compute (20) and (21), the spatial transformation ${}^1\boldsymbol{X}_G^T$ can be constructed by extracting the position of the CoM ${}^1\boldsymbol{p}_G$ from $\boldsymbol{H}$. First, note that the composite-rigid-body inertia (locked inertia) of the system $\boldsymbol{I}_1^C$ can be found within $\boldsymbol{H}_{11}$[23]

$$\boldsymbol{H}_{11} = \boldsymbol{\Phi}_1^T\boldsymbol{I}_1^C\boldsymbol{\Phi}_1. \tag{22}$$

This composite inertia has a well defined structure,[23] which allows the CoM position ${}^1\boldsymbol{p}_G$ to be extracted

$$\boldsymbol{I}_1^C = \boldsymbol{\Psi}_1^T\boldsymbol{H}_{11}\boldsymbol{\Psi}_1 \tag{23}$$

$$= \begin{bmatrix} \bar{\boldsymbol{I}}_1^C & M\,\boldsymbol{S}({}^1\boldsymbol{p}_G) \\ M\,\boldsymbol{S}({}^1\boldsymbol{p}_G)^T & M\,\boldsymbol{1} \end{bmatrix}, \tag{24}$$

where M is the total mass of the system.

Table 1 summarizes the procedure that can be used to compute $\boldsymbol{A}_G$ and $\dot{\boldsymbol{A}}_G\,\dot{\boldsymbol{q}}$ from knowledge of the floating-base kinematics, system mass matrix $\boldsymbol{H}$, and Coriolis term $\boldsymbol{C}\,\dot{\boldsymbol{q}}$ alone. Given these inputs, this short set of computations can be programmed in under 10 lines of code, and provides an $O(n)$ computation of the CMM and an $O(1)$ computation of the centroidal bias term. This compactness and efficiency represent improvements over previous specialized algorithms for the

Table 1. Computation summary.

Inputs: *Joint-Space Dynamics Descriptors:* $\boldsymbol{H}(\boldsymbol{q})$, $\boldsymbol{C}(\boldsymbol{q},\dot{\boldsymbol{q}})\,\dot{\boldsymbol{q}}$, $\boldsymbol{U}_1$
Floating-Base Kinematics: ${}^0\boldsymbol{R}_1(\boldsymbol{q}_1)$, $\boldsymbol{\Psi}_1(\boldsymbol{q}_1)$
Outputs: *Centroidal Dynamics Descriptors:* $\boldsymbol{A}_G$, $\dot{\boldsymbol{A}}_G\,\dot{\boldsymbol{q}}$
Computations:
$\boldsymbol{H}_{11} = \boldsymbol{U}_1\,\boldsymbol{H}\,\boldsymbol{U}_1^T$
$\boldsymbol{I}_1^C = \boldsymbol{\Psi}_1^T\boldsymbol{H}_{11}\boldsymbol{\Psi}_1$
$M = (\boldsymbol{I}_1^C)_{6,6}$
${}^1\boldsymbol{p}_G = \frac{1}{M}[(\boldsymbol{I}_1^C)_{3,5}\ (\boldsymbol{I}_1^C)_{1,6}\ (\boldsymbol{I}_1^C)_{2,4}]^T$
${}^i\boldsymbol{X}_G^T = \begin{bmatrix} {}^0\boldsymbol{R}_1 & {}^0\boldsymbol{R}_1\,\boldsymbol{S}({}^1\boldsymbol{p}_G)^T \\ \boldsymbol{0} & {}^0\boldsymbol{R}_1 \end{bmatrix}$
$\boldsymbol{A}_G = {}^i\boldsymbol{X}_G^T\boldsymbol{\Psi}_1^T\,\boldsymbol{U}_1\,\boldsymbol{H}$
$\dot{\boldsymbol{A}}_G\,\dot{\boldsymbol{q}} = {}^i\boldsymbol{X}_G^T\boldsymbol{\Psi}_1^T\,\boldsymbol{U}_1\,\boldsymbol{C}\,\dot{\boldsymbol{q}}$

centroidal dynamics. Note that, often, an effective choice for rigid-body simulation is to employ a selection of $\dot{\boldsymbol{q}}_1 = \mathbf{v}_1$ which gives $\boldsymbol{\Phi}_1 = \mathbf{1}_{6\times6}$. This choice further simplifies many aspects of the computation as

$$\boldsymbol{I}_1^C = \boldsymbol{H}_{11}, \tag{25}$$

$$\boldsymbol{A}_G = {}^i\boldsymbol{X}_G^T\, \boldsymbol{U}_1\, \boldsymbol{H}, \quad \text{and} \tag{26}$$

$$\dot{\boldsymbol{A}}_G\, \dot{\boldsymbol{q}} = {}^i\boldsymbol{X}_G^T\, \boldsymbol{U}_1\, \boldsymbol{C}\, \dot{\boldsymbol{q}}. \tag{27}$$

4. Application to a Dynamic Kicking Motion

This section describes the application of centroidal momentum control to a dynamic kicking motion. The CMM $\boldsymbol{A}_G$ and associated bias force $\dot{\boldsymbol{A}}_G\, \dot{\boldsymbol{q}}$ are used in whole-body control and are computed directly from the mass matrix $\boldsymbol{H}$ and Coriolis term $\boldsymbol{C}\dot{\boldsymbol{q}}$ in the joint-space dynamic equations of motion. Since the latter quantities are required in our whole-body controller, this results in more efficient computation for the CMM and bias force. Biomechanics studies suggest that the regulation of CAM may provide a target quantity to guide coordination between the upper-body and lower body.[3] This section demonstrates how CAM can be applied as a coordination target for humanoid robots, and discusses important considerations for its inclusion in whole-body control frameworks.

The kicking motion studied here is used to expand upon the role that centroidal momentum control plays within our previously introduced whole-body control framework.[7] This framework consists of a state machine coupled with a prioritized task-space controller. The state machine is used to sequence the system through the various phases of motion, as shown in Fig. 2. Prioritized task-space control (PTSC) is then applied to coordinate the many actuators of the humanoid and accomplish tracking of important features of the movement such as foot motion, CoM position, and CAM. We refer the reader to previous work[7] for full details, and focus attention to describe the centroidal momentum control aspects here.

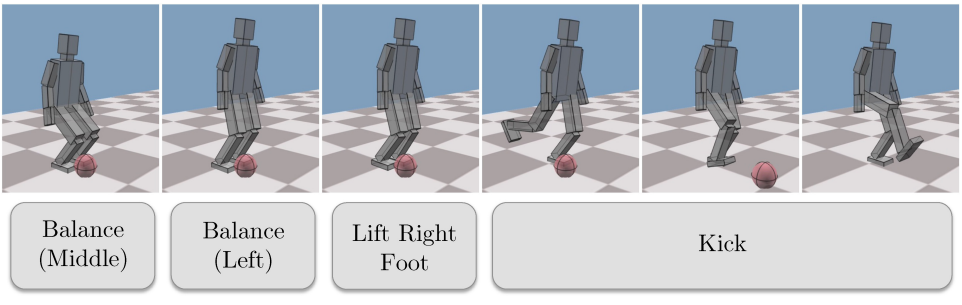

Fig. 2. Dynamic kicking motion and the four states of a finite state machine that compose its evolution. In the control approach, all state transitions are based on time.

4.1. *Centroidal momentum commands*

Rates of change in centroidal momentum are prescribed during each state of the motion to regulate the CoM position and CAM. For linear momentum, a commanded $\dot{\boldsymbol{l}}_{G,c}$ is formed from PD control on the desired CoM:

$$\dot{\boldsymbol{l}}_{G,c} = M[{}^0\ddot{\boldsymbol{p}}_{G,d} + \boldsymbol{K}_{D,\ell}({}^0\dot{\boldsymbol{p}}_{G,d} - {}^0\dot{\boldsymbol{p}}_G) + \boldsymbol{K}_{P,\ell}({}^0\boldsymbol{p}_{G,d} - {}^0\boldsymbol{p}_G)]. \tag{28}$$

The desired CoM trajectory for ${}^0\boldsymbol{p}_G$ is prescribed based on a set of simple third-order Bézier curves. The commanded rate of change in angular momentum takes a simpler form:

$$\dot{\boldsymbol{k}}_{G,c} = \dot{\boldsymbol{k}}_{G,d} + \boldsymbol{K}_{D,k}(\boldsymbol{k}_{G,d} - \boldsymbol{k}_G). \tag{29}$$

The desired CAM trajectory $\boldsymbol{k}_{G,d}$ can be selected heuristically to encode a desired whole-body rotation about a given axis. During all states except the Kick state, $\boldsymbol{k}_{G,d}$ is set to zero. During the Kick state, this setpoint is formed based on the desired dynamics of the kicking leg. The foot trajectory itself is specified through trajectories on a virtual leg length r and angle θ.

The desired evolution of the virtual leg angle θ is then used to specify a desired CAM as follows. Throughout the example, the inertial z-axis is opposite gravity and the y-axis is perpendicular to the sagittal plane. To encode a whole-body rotation about the y-axis, the system's net moment of inertia about the y-axis I_{yy} is recorded at the beginning of the kick. This can be found from the mass matrix, by first computing the composite-rigid-body inertia of the system $\boldsymbol{I}_G$ about the CoM

$$\boldsymbol{I}_G = {}^i\boldsymbol{X}_G^T \boldsymbol{\Psi}_1^T \boldsymbol{H}_{11} \boldsymbol{\Psi}_1 {}^1\boldsymbol{X}_G, \tag{30}$$

$$= \begin{bmatrix} \bar{\boldsymbol{I}}_G & \boldsymbol{0} \\ \boldsymbol{0} & M\,\boldsymbol{1} \end{bmatrix}, \tag{31}$$

and then selecting the desired component of the cartesian inertia

$$I_{yy} = (\bar{\boldsymbol{I}}_G)_{(2,2)}. \tag{32}$$

The desired CAM and its rate are then selected as:

$$\boldsymbol{k}_{G,d} = [0, \gamma I_{yy}\dot{\theta}_d, 0]^T,$$
$$\dot{\boldsymbol{k}}_{G,d} = [0, \gamma I_{yy}\ \ddot{\theta}_d, 0]^T.$$

By employing a non-zero angular momentum setpoint for the pitch, this selection encodes a desired whole-body pitch rotation. During the kicking motion, the kicking leg produces a large amount of pitch angular momentum. Thus, if γ is close to zero, tracking $\boldsymbol{k}_{G,d} \approx \boldsymbol{0}$ requires upper-body motions to produce pitch momentum opposite that of the kicking leg. When γ is a large positive value, tracking $\boldsymbol{k}_{G,d}$ requires upper-body motions to contribute additional pitch angular momentum of the same sign as the kicking leg. Nominally, we employ $\gamma = 0.8$ to encode that we desire 80% of the system inertia to be producing pitch angular momentum in sync with the kicking leg.

This proportion approximately represents the percentage of the system inertia in the upper-body and kicking leg combined. The role of γ will be explored further in Sec. 4.3. Although very simple, the use of this desired angular momentum trajectory will be shown to be an effective strategy to encode whole-body motion.

4.2. *Centroidal momentum within task-space control*

Given the commanded rate of change in centroidal momentum, TSC is applied to realize this command in the humanoid. Although there are other approaches to include centroidal momentum control within whole-body frameworks,[5,25] the wide use of TSC and its general applicability motivates its adoption in this example. TSC seeks to find whole-body joint torques which minimize the deviation from some commanded task acceleration $\dot{\boldsymbol{v}}_{t,c}$. Examining (11), the CMM provides a Jacobian-like relationship, similar to that between joint rates and a traditional task-space (or operational-space) velocity. As a result, the inclusion of a commanded rate of change in centroidal momentum fits cleanly within this framework.

In order to address limitations on ground reaction forces, the TSC problem is formulated as a constrained optimization problem. This optimization problem can be formulated over dynamic variables of torques $\boldsymbol{\tau}$, $\ddot{\boldsymbol{q}}$, and ground reaction forces $\boldsymbol{f}_s$, where the consistency of these variables with the system dynamics must be enforced.

$$\min_{\ddot{\boldsymbol{q}},\boldsymbol{\tau},\boldsymbol{f}_{s_{ij}}} \quad \frac{1}{2}\|\boldsymbol{J}_t\,\ddot{\boldsymbol{q}} + \dot{\boldsymbol{J}}_t\,\dot{\boldsymbol{q}} - \dot{\boldsymbol{v}}_{t,c}\|^2 + \frac{1}{2}\|\boldsymbol{A}_G\,\ddot{\boldsymbol{q}} + \dot{\boldsymbol{A}}_G\,\dot{\boldsymbol{q}} - \dot{\mathbf{h}}_{G,c}\|^2, \tag{33}$$

$$\text{subject to } \boldsymbol{H}\,\ddot{\boldsymbol{q}} + \boldsymbol{C}\,\dot{\boldsymbol{q}} + \boldsymbol{G} = \boldsymbol{S}_a^T\boldsymbol{\tau} + \sum_{i=1}^{N_S}\sum_{j=1}^{N_{P_i}} \boldsymbol{J}_{s_{ij}}^T\boldsymbol{f}_{s_{ij}}, \tag{34}$$

$$\boldsymbol{f}_{s_{ij}} \in \mathcal{C}_i \quad \forall\, i \in \{1,\ldots,N_S\},\, j \in \{1,\ldots,N_{P_i}\}. \tag{35}$$

Here $\boldsymbol{J}_t$ is a task Jacobian, $\boldsymbol{S}_a = [\mathbf{0}_{n\times 6}\ \mathbf{1}_{n\times n}]$ is the actuated joint selector, $\boldsymbol{J}_{s_{ij}}$ is a Jacobian for contact vertex j of foot i,[26] and $\mathcal{C}_i$ is a friction cone for foot i. N_S provides the number of feet in support, and N_{P_i} is the number of contact vertices for foot i. $\boldsymbol{J}_t$ may be a Jacobian for a set of tasks and may include, for instance, foot and pose Jacobians within its rows. In essence, the optimization problem is formulated for the humanoid to track the desired task dynamics as closely as possible while satisfying constraints on its interactions with the ground through contact.

Similarly structured frameworks, some under the names of task-space inverse dynamics, have demonstrated the capacity of this optimization-based whole-body control approach to address joint torque limits,[7] joint angle limits,[27] and self-collision[28] as well. In practice, variables for torque $\boldsymbol{\tau}$ or acceleration $\ddot{\boldsymbol{q}}$ can be removed from these formulations to accelerate their performance.[7,8] In this work, $\ddot{\boldsymbol{q}}$ is removed by expressing $\ddot{\boldsymbol{q}}$ as a function of $\boldsymbol{\tau}$ and $\boldsymbol{f}_{s_{ij}}$ through (34). The formulation is solved with the conic interior-point solver of MOSEK,[29] and performs at rates of 250 Hz which are sufficient for real-time simulation.

Table 2. Weight and gain settings for the PTSC. Where omitted, all derivative gains are set for critical damping. All kinematic tasks employ a command of the form $\ddot{x}_c = \ddot{x}_d + K_P(x_d - x) + K_D(\dot{x}_d - \dot{x})$.

Task	Weight	K_P (s^{-2})	Priority
Linear momentum (CoM)	200	30	2
Angular momentum	100	$K_D = 25\,\mathrm{s}^{-1}$	3
Torso orientation	(100, 100, 25)	120	3
Hip	1	40	3
Knee	0.1	120	3
Ankle	0.1	120	3
Shoulder	10	220	3
Elbow	10	240	3
Foot position and orientation	1	50	1

Often, a strict hierarchy of importance exists amongst the tasks. When this is the case, the TSC problem is instead a PTSC problem.[7] For instance, in the kicking example, the foot accelerations are set as the highest priority, while the CoM acceleration is the second highest. In the null space of these tasks, the CAM and pose are regulated. For comparison later in the text, we describe this prioritization using the ">" operator, with the prioritization used here denoted as $(feet) > (CoM) > (CAM\ and\ pose)$. Within each priority level, task Jacobians and commands are multiplied by weighting factors to specify relative importance when a strict preference is not desired. To solve a PTSC problem, the above optimization problem may be solved multiple times in a cascaded fashion, first for the highest priority task. Then, subsequent solves for lower-priority tasks can be carried out with additional constraints to preserve the tracking optimality of the previous levels. Further details on the exact implementation of this hierarchical approach can be found in our previous publication.[7] Other more sophisticated techniques that embed the hierarchy into a single optimization problem have also been proposed and shown computational benefits.[30]

4.3. *Results*

This whole-body control approach was applied in simulation to a small humanoid model. The model, shown in Fig. 2, has 26 DoF and a mass distribution modeled after a 50th percentile male.[31] Total mass and height are $M = 19.12$ kg and $h = 1.05$ m. The task-space weights and gains for this system are shown in Table 2.[b] Simulation is carried out with the DynaMechs[32] simulation package, which employs a penalty-based spring-damper model of contact. Contact for each foot with the ground is

[b]Note that the task-space gains effectively encode desired time constants for the task-space error dynamics. As a result, for scaled versions (in mass or size) of the same system, these values require no retuning. However, task weightings do require modification since linear and angular momentum scale as Mh and Mh^2, respectively, while kinematic tasks scale only with h. Thus, to achieve comparable results on scaled versions of the same system with new mass $\tilde{M}$ and height $\tilde{h}$, linear and angular momentum weights can be scaled by $Mh/\tilde{M}\tilde{h}$ and $Mh^2/\tilde{M}\tilde{h}^2$, and kinematic task weights by $h/\tilde{h}$.

Table 3. Timing for computation of centroidal momentum quantities.

Quantity	Algorithm	Order	Time (μs)
$\boldsymbol{H}$	CRBA[23]	$O(n^2)$	75.8
$\boldsymbol{C}\dot{\boldsymbol{q}}$	RNEA[23]	$O(n)$	26.8
$\boldsymbol{A}_G$	CMM recursive[1]	$O(n)$	63.2
	Table 1	$O(n)$	10.5
$\dot{\boldsymbol{A}}_G\,\dot{\boldsymbol{q}}$	Finite difference	$O(n)$	63.9
	Table 1	$O(1)$	0.8

modeled through four point contacts considered at the support vertices on the bottom of the foot. Static and kinetic friction coefficients of $\mu_s = 0.95$ and $\mu_k = 0.6$ are used in the majority of the simulation experiments. Optimized joint torques $\boldsymbol{\tau}$ from (33) are computed at a control loop rate of 250 Hz and are applied directly to the humanoid joints for simulation.

Computation times for the centroidal quantities $\boldsymbol{A}_G$ and $\dot{\boldsymbol{A}}_G\,\dot{\boldsymbol{q}}$ with this model are provided in Table 3. Computation times for the mass matrix $\boldsymbol{H}$ and the Coriolis bias force $\boldsymbol{C}\,\dot{\boldsymbol{q}}$ are also shown for comparison. When $\boldsymbol{H}$ and $\boldsymbol{C}\,\dot{\boldsymbol{q}}$ are required elsewhere for whole-body control, this table shows significant computational benefits when applying the new computations for the CMM and its bias term using the simple algorithm summarized in Table 1. For the CMM computation, both the original specialized CMM algorithm by Orin *et al.*[1] and the computation of $\boldsymbol{A}_G$ in Table 1 require $O(n)$ operations. The relatively more involved computations in each recursive step of the original CMM algorithm enables our new computation here to be executed in a sixth of the time despite having the same computational order. To compute the CMM bias, the new computations proposed in Table 1 enjoy both improved order and computation time in comparison to the fastest previous method to compute $\dot{\boldsymbol{A}}_G\,\dot{\boldsymbol{q}}$. In fact, even when $\boldsymbol{C}\,\dot{\boldsymbol{q}}$ has yet to be computed, the method to compute $\dot{\boldsymbol{A}}_G\,\dot{\boldsymbol{q}}$ in Table 1 is faster than an inexact finite-difference method.

To demonstrate the effects of controlling the CAM, the whole-body task-space approach was first applied with CAM control turned off, providing a prioritization order of $(feet) > (CoM) > (pose)$. The pose task was applied with a desired torso orientation and desired joint angles for a relaxed standing posture. The kick motion was applied with a soccer ball modeled as an infinitely thin spherical shell with mass 0.12 kg and radius 7 cm (roughly, a FIFA standard soccer ball normalized to the mass and height of the humanoid). Contact forces were modeled between the foot and the ball using an elastic model of contact. No knowledge of the contact forces was provided to the task-space controller, and thus this interaction represented a disturbance to the system. Snapshots from the resultant motion are shown in Fig. 2, with a video provided in the supplementary material available at

https://www.go.osu.edu/WensingOrin-IJHR_WBC_SI.

While the behavior maintains balance with the CAM control turned off, it displays a lack of upper-body motion due to the tasks employed.

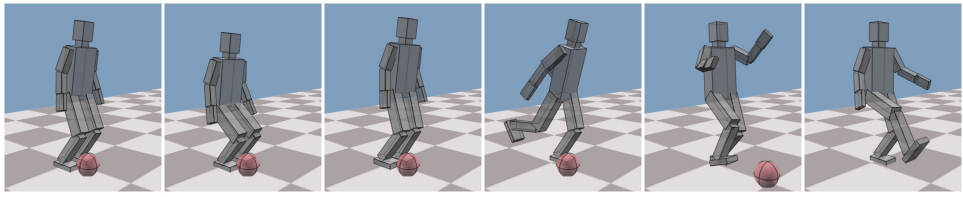

Fig. 3. Snapshots of the dynamic kicking motion when CAM control is turned on. In comparison to the previous example, the system displays emergent upper-body motions through a simple selection of desired angular momentum setpoints.

This simple example was repeated, with CAM control enabled at the lowest priority level, providing a prioritization of $(feet) > (CoM) > (CAM\ and\ pose)$. Figure 3 shows the whole-body motion that results. Simply through the prescription of a commanded CAM, the humanoid displays rich upper-body motion.

The parameter γ, which controls the magnitude of the pitch angular momentum in relation to the kick leg speed, provides further capability to shape the upper-body motion. Figure 4 and the supplementary video show the resultant upper-body motion as γ is varied. In the case when $\gamma = 0.8$, the upper-body performs motions that produce pitch angular momentum in addition to that of the kick leg, resulting in a coordinated and balanced whole-body rotation. Figure 4 shows that the left arm has more emergent movement than the right for $\gamma = 0.8$. This motion is coordinated by the controller to cancel the yaw momentum created by the kicking leg. Figure 5 shows the yaw CAM composition during the kicking state of the motion. The yaw angular momentum contribution from the upper-body cancels out a large portion of

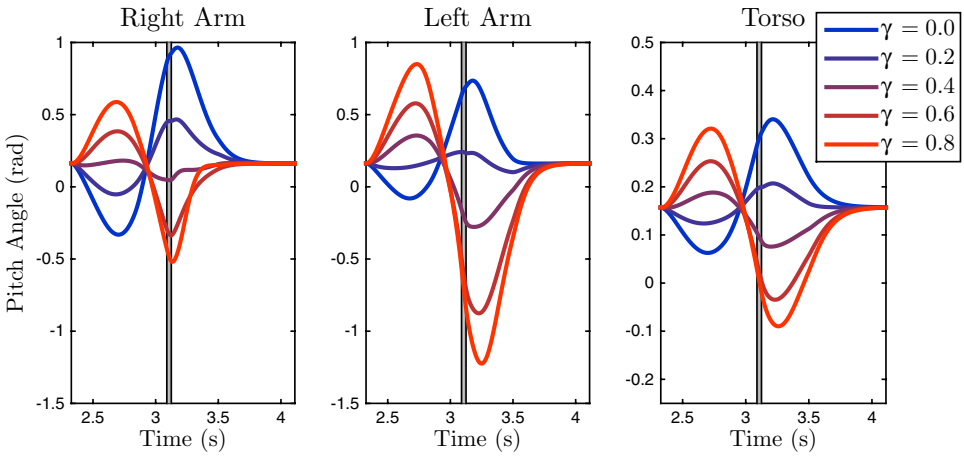

Fig. 4. Variation in the pitch angle evolution during the kicking state with changes in γ. Pitch angles are given about the lateral axis which points away from the left side of the body. The period of contact with the ball around $t = 3.1$ s is shaded in each plot. Further details on the contributions of these movements to pitch and yaw momentum are provided in Fig. 6.

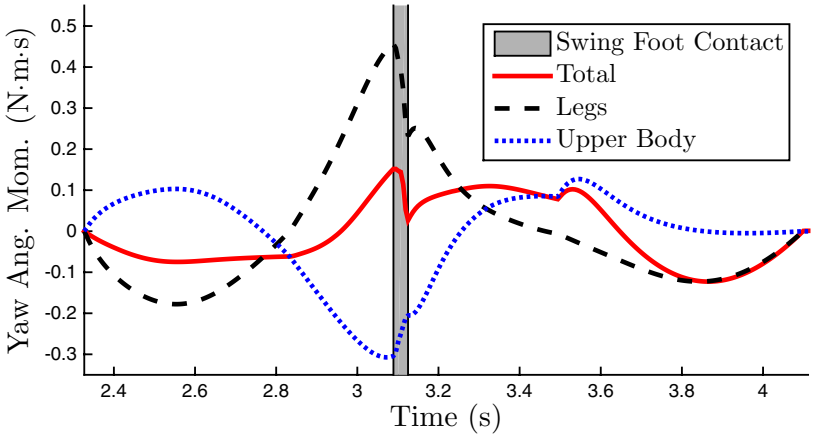

Fig. 5. Centroidal yaw angular momentum and composition during the Kick state of the dynamic kicking motion for $\gamma = 0.8$. The upper-body motions provide a partial cancelation of the angular momentum contributions of the legs. The rapid change in yaw momentum during the middle of the kick is due to contact interaction with the ball, which exerts a net negative yaw angular impulse on the system.

the yaw angular momentum contribution of the legs, canceling 67% during the most dynamic part of the kick.

Similar yaw momentum cancelations are observed when $\gamma = 0.0$ is employed by the controller. Figure 6 highlights that these yaw momentum cancelations occur across different selections of γ. Note that when $\gamma = 0.0$, the upper-body acts to partially cancel pitch angular momentum created from the kick as shown in Fig. 6. In order to accomplish this, the arms instead swing opposite the kicking leg right before impact. To simultaneously regulate yaw however, the right arm must move more dynamically than the left, as shown in Fig. 4 and in contrast to when $\gamma = 0.8$. These intersegmental yaw momentum cancelations emerge automatically without needing

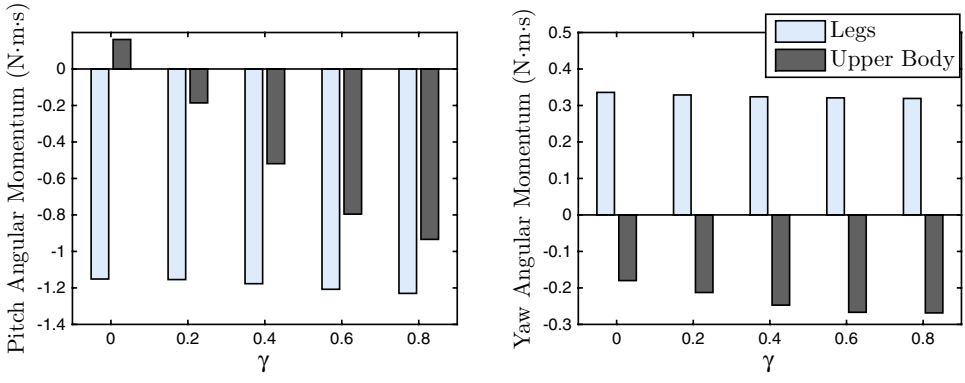

Fig. 6. Angular momentum contributions from the upper-body and legs as γ is varied. Angular momentum is measured at $t = 3.0$ s, which is approximately 100 ms prior to swing leg contact with the ball.

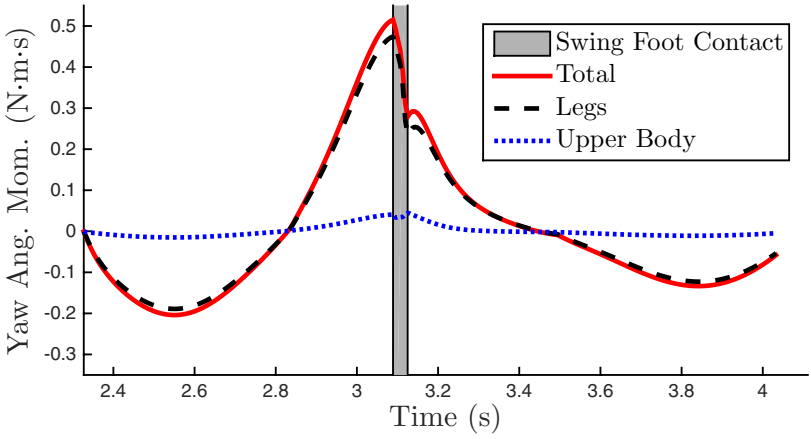

Fig. 7. Centroidal yaw angular momentum and composition during the Kick state of the dynamic kicking motion *without* CAM control.

to retune any other controller parameters. When no CAM control is applied, however, the total yaw angular momentum is not well regulated and matches that of the legs, as shown in Fig. 7.

These yaw momentum cancelations are desirable features for the whole-body controller. The momentum cancelations due to the upper-body motions decrease the net yaw momentum, and also decrease the net yaw moment about the CoM. This net yaw moment about the CoM is closely linked to the yaw moment under the stance foot. Defining $\boldsymbol{n}_G \in \mathbb{R}^3$ as the net moment about the CoM, $\boldsymbol{n}_G$ is related to the net force $\boldsymbol{f} \in \mathbb{R}^3$ and ground normal (yaw) moment $n_z \in \mathbb{R}$ about the center of pressure (CoP) as

$$\dot{\boldsymbol{k}}_G = \boldsymbol{n}_G = \begin{bmatrix} 0 \\ 0 \\ n_z \end{bmatrix} + (\boldsymbol{p}_{CoP} - \boldsymbol{p}_G) \times \boldsymbol{f}, \tag{36}$$

where $\boldsymbol{p}_{CoP} \in \mathbb{R}^3$ is the position of the CoP under the foot. In motions with small CoM accelerations, $\boldsymbol{f} \approx [0, 0, Mg]^T$, and thus the force itself does not create a large yaw moment about the CoM. In this case, the rate of change in centroidal yaw momentum is approximately equal to the normal (yaw) moment under the foot (about the CoP).

When no CAM control is applied for the kick, the rapid accelerations of the swing leg lead to rapid changes in centroidal yaw momentum. In this case, the average yaw moment under the foot is 0.9391 Nm with a maximum of 2.801 Nm. However, when CAM control is applied, the upper-body motions partially cancel the yaw momentum of the legs, leading in turn to smaller rates of change in net yaw momentum. Thus, when CAM control is applied, the yaw moment under the foot is decreased to 0.5447 Nm with a maximum of 1.981 Nm at mid-kick.

These yaw moments under the foot are created by tangential forces distributed underneath the foot that, in ensemble, create moments. Thus, this reduction in yaw moment through CAM control has the desirable effect of reducing the frictional requirement of the kick. This effect causes the system to be more robust to errors in the assumed contact model by providing increased margin to remain within the friction cones in comparison to when no CAM control is applied. This margin also has potential benefit to the case of contact disturbances, when disturbances may temporarily shift the system into a regime of kinetic (reduced) friction. While only studied for standing balance here, the regulation of yaw momentum has also proved to be of utility in dynamic locomotion.[17]

The supplemental video to this paper illustrates this benefit further, in the case of limited friction. The friction coefficients for simulation are limited to half of their nominal value ($\mu_s = 0.475$, $\mu_k = 0.3$), while the controller continues to assume that the environment has the original friction values ($\mu_s = 0.95$, $\mu_k = 0.6$). The case of no CAM control results in significant foot slip. However, when CAM control is used, its lower frictional requirements make it robust to this change in the environment. The results for this lower environmental friction have no perceptible differences with the original results when CAM control is used.

The role of upper-body motion in regulating the yaw moment has been noted in human biomechanics[33] and humanoid gait planning[34,35] work as well. Park[33] showed how arm swing during walking can result by limiting the allowable yaw moment under the foot. Ugurlu *et al.*[34] showed how a rigid torso can be employed to compensate for the required yaw moment from the legs. The CAM control approach here coordinates all of the arm DoFs to accomplish a similar aim without having to constrain the yaw moment explicitly.

4.4. *Implementation of centroidal angular momentum control*

CAM control is an emerging approach, with a growing number of application examples available in the literature. Fewer, though, are its applications to very dynamic movements. While the new relationships with the joint-space equations of motion, developed here, simplify application of centroidal momentum control, careful CAM control integration is still important for the whole-body control system to perform as desired. The selection of proper setpoints as well as prioritization are particularly important details. In the previous sections and in our previous work, we have presented design decisions for CAM control which have provided dynamic whole-body movements. Drawing on our experience applying CAM control for balance and locomotion, this section provides further discussion on the consequences of alternate design decisions which can often lead to surprising results.

Previous work has utilized $\boldsymbol{k}_{G,d} = \mathbf{0}$ in their implementations of CAM control.[11,36] While this setpoint works well for standing balance, faster movements, such as the kick considered here may require a more dynamic desired angular momentum. The effect of employing $\boldsymbol{k}_{G,d} = \mathbf{0}$ is shown in Fig. 8, and results in pitching motions in

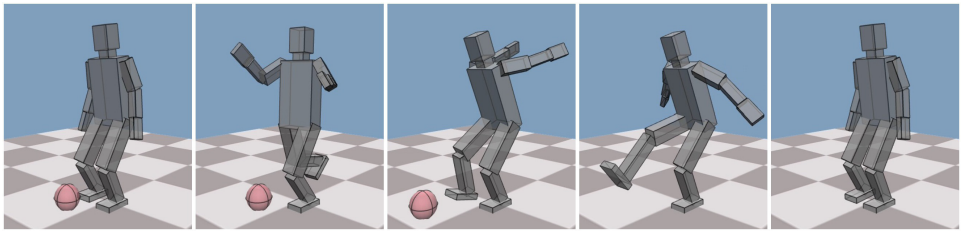

Fig. 8. Dynamic kicking motion when $\boldsymbol{k}_{G,d} = \mathbf{0}$. The CAM weight in the task-space controller was doubled to emphasize its effect for this case. Here, the torso pitches backwards at the beginning of the kick to cancel the change in angular momentum from the backward movement of the swing leg. Overall, the upper-body motion displays counter-rotational movements when compared to Fig. 3.

the torso opposite to that of the swing leg in order to cancel its pitch angular momentum effects. In motions, such as running,[17] which include significant swing-leg dynamics, this undesired torso pitching can be an even larger issue if the pitch CAM task weighting is selected too high or an appropriate setpoint is not prescribed.

Other whole-body control strategies have explicitly prioritized the CAM control task over other objectives in a whole-body control system.[11] But to what extent should the CAM be prioritized in a TSC framework? From our experiments with CAM in whole-body control we have developed a few rules of thumb. In the PTSC framework, placing the CAM control task at a priority above the CoM can unnecessarily constrain the achievable dynamics of the humanoid, and effectively enforces a nonholonomic virtual constraint on the system. Also, in the examples shown here, regardless of the CAM setpoint, a prioritization order of $(feet) > (CAM) > (CoM) > (pose)$ led to rapid upper-body instability.

A modified prioritization order of $(feet) > (CAM\ and\ CoM) > (pose)$ intuitively seems most reasonable, as the CAM and CoM dynamics together define the net external forces. The results of this strategy, however, show the importance of regularizing the CAM task by a desired pose. Figure 9 and the video supplement show the effects of this prioritization. Although small CAM control errors would typically allow the system to return to a nominal upper-body posture at the end of the motion, explicit CAM prioritization over pose undesirably restricts the system in this case. Due to the nonholonomic character of the centroidal momentum, there is no desired "average system orientation" included in the CAM control law Eq. (29), and thus CAM control benefits from regularization by the pose task when placed at the same priority level. These observations discourage the strict prioritization of CAM control in prioritized whole-body control frameworks.[c]

The prioritization scheme for the centroidal linear momentum, in contrast, has much less effect on the system performance. While the prioritization order $(feet) > (CoM) > (CAM\ and\ pose)$ was employed in the main results of this paper, the

[c] As a counterexample to this rule of thumb, CAM prioritization may be desirable in stance periods prior to prolonged flight, such as encountered in a running jump.[37] In these cases, poor regulation of the CAM prior to liftoff can have a severe impact on the ability to maintain an upright posture in flight.

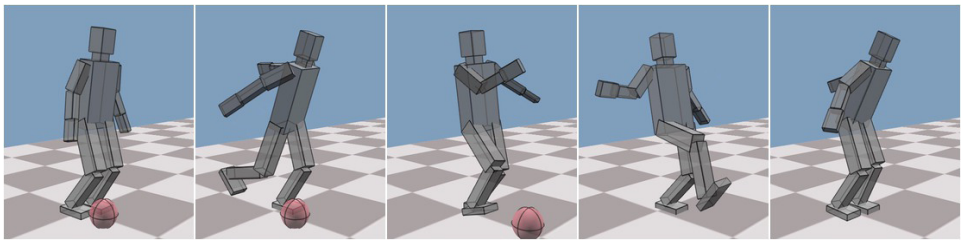

Fig. 9. Motion snapshots with a task prioritization of $(feet) > (CAM\ and\ CoM) > (pose)$ and $\gamma = 0.6$. With the CAM task at a higher priority than the pose, larger arm motions result. Perhaps surprisingly, prioritized CAM control effectively places an unnecessary nonholonomic constraint on the system and prevents convergence to an attainable nominal upper-body pose.

whole-body control performs comparably for the prioritization $(feet) > (CoM, CAM, and\ pose)$ with proper weighting of the CoM. While it may seem counterintuitive to ever consider placing the linear and angular portions of the momentum controller at different priority levels, we note that linear and angular momentum of the system are not completely analogous. While the centroidal linear momentum has a well-known connection to the velocity of the CoM, the nonholonomic character of the angular momentum[38] precludes any similar relationship to a notion of an average system orientation. Due to the stronger connection of the linear momentum to the CoM, much previous work has described the benefits of sacrificing angular momentum tracking specifically to improve CoM regulation.[5,39,40] Still, it appears that the use of a weighting or prioritization strategy for the CoM is an open selection for the whole-body control designer.

5. Conclusion

While previous studies have presented specialized algorithms to compute the CMM and the centroidal momentum velocity-dependent bias force, this work has shown how an improved set of computations can be used to obtain these centroidal quantities from the structural components of the dynamic equations of motion. When the system mass matrix and Coriolis force are available, only the kinematics of the floating-base are needed as an input to our new procedure which computes the CMM and bias force. When these joint-space quantities have already been obtained for whole-body control, these results represent an improvement beyond previous specialized methods in terms of the general applicability of the computations as well as their compactness and computational efficiency.

An expanded example of whole-body control for a dynamic kick has demonstrated the integration of centroidal momentum control into a whole-body framework, and highlighted the power of this approach to ease whole-body motion authoring through the prescription of angular momentum setpoints. The emergent upper-body motions afforded through CAM control provide reduced yaw moments at the ground contact, decreasing the potential for foot slip in comparison to when no CAM control strategy

is applied. With the insights provided here and the new procedure to compute the centroidal dynamics, the incorporation of centroidal momentum control can be a more accessible goal for future whole-body control approaches.

Acknowledgments

This work was supported in part by a fellowship from the National Science Foundation to Patrick Wensing. Other funding was provided by Grant No. CNS-0960061 from the National Science Foundation with a subaward to The Ohio State University.

References

1. D. E. Orin, A. Goswami and S.-H. Lee, Centroidal dynamics of a humanoid robot, *Auton. Robots* **35**(2) (2013) 161–176.
2. D. E. Orin and A. Goswami, Centroidal momentum matrix of a humanoid robot: Structure and properties, in *IEEE/RSJ Int. Conf. on Intelligent Robots and Systems* (Nice, France, 2008), pp. 653–659.
3. H. Herr and M. Popovic, Angular momentum in human walking, *J. Exp. Biol.* **211**(4) (2008) 467–481.
4. A. Macchietto, V. Zordan and C. R. Shelton, Momentum control for balance, in *ACM SIGGRAPH 2009* (New Orleans, Louisiana, 2009), pp. 80:1–8.
5. S.-H. Lee and A. Goswami, A momentum-based balance controller for humanoid robots on non-level and non-stationary ground, *Auton. Robots* **33**(4) (2012) 399–414.
6. M. de Lasa, I. Mordatch and A. Hertzmann, Feature-based locomotion controllers, in *ACM SIGGRAPH 2010* (Los Angeles, California, 2010), pp. 131:1–10.
7. P. M. Wensing and D. E. Orin, Generation of dynamic humanoid behaviors through task-space control with conic optimization, in *IEEE Int. Conf. on Robotics and Automation* (Karlsruhe, Germany, 2013), pp. 3103–3109.
8. A. Herzog, L. Righetti, F. Grimminger, P. Pastor and S. Schaal, Balancing experiments on a torque-controlled humanoid with hierarchical inverse dynamics, in *IEEE/RSJ Int. Conf. on Intelligent Robots and Systems* (Chicago, IL, 2014), pp. 981–988.
9. H. Dai, A. Valenzuela and R. Tedrake, Whole-body motion planning with centroidal dynamics and full kinematics, in *IEEE-RAS Int. Conf. Humanoid Robots* (Madrid, Spain, 2014), pp. 295–302.
10. S. Kajita, F. Kanehiro, K. Kaneko, K. Fujiwara, K. Harada, K. Yokoi and H. Hirukawa, Resolved momentum control: Humanoid motion planning based on the linear and angular momentum, in *Proc. IEEE/RSJ Int. Conf. on Intelligent Robots and Systems* (Las Vegas, USA, 2003), pp. 1644–1650.
11. B. J. Stephens and C. G. Atkeson, Dynamic balance force control for compliant humanoid robots, in *IEEE/RSJ Int. Conf. on Intelligent Robots and Systems* (Taipei, Taiwan, 2010), pp. 1248–1255.
12. S. Kajita, F. Kanehiro, K. Kaneko, K. Fujiwara, K. Harada, K. Yokoi and H. Hirukawa, Biped walking pattern generation by using preview control of zero-moment point, in *Proc. IEEE Int. Conf. Robotics and Automation (ICRA)* (Taipei, Taiwan, 2003), pp. 1620–1626.
13. T. Buschmann, R. Wittmann, M. Schwienbacher and H. Ulbrich, A method for real-time kineto-dynamic trajectory generation, in *IEEE-RAS Int. Conf. Humanoid Robots (Humanoids)* (Osaka, Japan, 2012), pp. 190–197.

14. J. Mayr, H. Gattringer and H. Bremer, A bipedal walking pattern generator that considers multi-body dynamics by angular momentum estimation, in *IEEE-RAS Int. Conf. Humanoid Robots (Humanoids)* (Osaka, Japan, 2012), pp. 177–182.
15. M. Popovic, A. Hofmann and H. Herr, Angular momentum regulation during human walking: Biomechanics and control, in *IEEE Int. Conf. on Robotics and Automation* (New Orleans, Louisiana, 2004), pp. 2405–2411.
16. Y. Ye and C. K. Liu, Optimal feedback control for character animation using an abstract model, in *ACM SIGGRAPH 2010* (New York, NY, USA, 2010), pp. 74:1–9.
17. P. M. Wensing and D. E. Orin, High-speed humanoid running through control with a 3D-SLIP model, in *Proc. IEEE/RSJ Int. Conf. on Intelligent Robots and Systems* (Tokyo, Japan, 2013), pp. 5134–5140.
18. M. Al Borno, E. Fiume, A. Hertzmann and M. de Lasa, Feedback control for rotational movements in feature space, *Comput. Graph. Forum* **33**(2) (2014) 225–233.
19. V. Zordan, D. Brown, A. Macchietto and K. Yin, Control of rotational dynamics for ground and aerial behavior, *IEEE Trans. Vis. Comput. Graphics* **20**(10) (2014) 1356–1366.
20. J. Ostrowski and J. Burdick, Geometric perspectives on the mechanics and control of robotic locomotion, in *Robotics Research*, eds. G. Giralt and G. Hirzinger (Springer London, UK, 1996), pp. 536–547.
21. P.-B. Wieber, Holonomy and nonholonomy in the dynamics of articulated motion, in *Fast Motions in Biomechanics and Robotics*, eds. M. Diehl and K. Mombaur (Springer Berlin, Berlin/Heidelberg/New York, 2006), pp. 411–425.
22. R. Featherstone, *Rigid Body Dynamics Algorithms* (Springer, New York, 2008).
23. R. Featherstone and D. Orin, Dynamics, in *Springer Handbook of Robotics*, Chap. 2, eds. B. Siciliano and O. Khatib (Springer, New York, 2008).
24. R. E. Roberson and R. Schwertassek, *Dynamics of Multibody Systems* (Springer-Verlag, Berlin/Heidelberg/New York, 1988).
25. F. Moro, M. Gienger, A. Goswami, N. Tsagarakis and D. Caldwell, An attractor-based whole-body motion control (WBMC) system for humanoid robots, in *IEEE-RAS Int. Conf. on Humanoid Robots* (Atlanta, Georgia, USA, 2013), pp. 42–49.
26. P. M. Wensing, G. B. Hammam, B. Dariush and D. E. Orin, Optimizing foot centers of pressure through force distribution in a humanoid robot, *Int. J. Human. Robot.* **10**(3) (2013) 350027:1–21.
27. L. Saab, N. Mansard, F. Keith, J.-Y. Fourquet and P. Soueres, Generation of dynamic motion for anthropomorphic systems under prioritized equality and inequality constraints., in *IEEE Int. Conf. on Robotics and Automation* (Shanghai, China, 2011), pp. 1091–1096.
28. J. Vaillant, A. Kheddar, H. Audren, F. Keith, S. Brossette, K. Kaneko, M. Morisawa, E. Yoshida and F. Kanehiro, Vertical ladder climbing by the HRP-2 humanoid robot, in *IEEE-RAS Int. Conf. Humanoid Robots (Humanoids)* (Madrid, Spain, 2014), pp. 671–676.
29. E. D. Andersen, C. Roos and T. Terlaky, On implementing a primal-dual interior-point method for conic quadratic optimization, *Math. Program.* **95**(1) (2003) 249–277.
30. A. Escande, N. Mansard and P.-B. Wieber, Hierarchical quadratic programming: Fast online humanoid-robot motion generation, *Int. J. Robot. Res.* **33**(7) (2014) 1006–1028.
31. D. A. Winter, *Biomechanics and Motor Control of Human Movement* 2nd edn. (John Wiley & Sons, New York, 1990).
32. S. McMillan, D. E. Orin and R. B. McGhee, DynaMechs: An object oriented software package for efficient dynamic simulation of underwater robotic vehicles, in *Underwater Robotic Vehicles: Design and Control* (TSI Press, Albuquerque, NM, 1995), pp. 73–98.

33. J. Park, Synthesis of natural arm swing motion in human bipedal walking, *J. Biomech.* **41**(7) (2008) 1417–1426.
34. B. Ugurlu, J. A. Saglia, N. G. Tsagarakis and D. G. Caldwell, Yaw moment compensation for bipedal robots via intrinsic angular momentum constraint, *Int. J. Human. Robot.* **09**(04) (2012) 1250033:1–27.
35. M. Schwienbacher, T. Buschmann, S. Lohmeier, V. Favot and H. Ulbrich, Self-collision avoidance and angular momentum compensation for a biped humanoid robot, in *IEEE Int. Conf. on Robotics and Automation (ICRA)* (Shanghai, China, 2011), pp. 581–586.
36. S.-H. Lee and A. Goswami, Ground reaction force control at each foot: A momentum-based humanoid balance controller for non-level and non-stationary ground, in *IEEE Int. Conf. on Intelligent Robots and Systems* (Taipei, Taiwan, 2010), pp. 3157–3162.
37. P. M. Wensing and D. E. Orin, Development of high-span running long jumps for humanoids, in *IEEE Int. Conf. on Robotics and Automation* (Hong Kong, 2014), pp. 222–227.
38. Y. Nakamura and R. Mukherjee, Nonholonomic path planning of space robots, in *IEEE Int. Conf. on Robotics and Automation* (Scottsdale, AZ, 1989), pp. 1050–1055.
39. A. Hofmann, M. Popovic and H. Herr, Exploiting angular momentum to enhance bipedal center-of-mass control, in *IEEE Int. Conf. on Robotics and Automation* (Kobe, Japan, 2009), pp. 4423–4429.
40. J. Pratt, J. Carff, S. Drakunov and A. Goswami, Capture point: A step toward humanoid push recovery, in *IEEE-RAS Int. Conf. on Humanoid Robots* (Genova, Italy, 2006), pp. 200–207.

Patrick M. Wensing received his B.S., M.S. and Ph.D. degrees in Electrical and Computer Engineering from The Ohio State University in 2009, 2013, and 2014, respectively. Dr. Wensing was awarded a National Science Foundation Graduate Research Fellowship for his graduate studies. He is currently a Postdoctoral Associate in the Department of Mechanical Engineering at the Massachusetts Institute of Technology, working under Sangbae Kim on the MIT Cheetah project. Dr. Wensing's research interests lie broadly in the areas of applied optimization and control theory for legged robotic systems. He served as the cochair of the IEEE Robotics and Automation Society Student Activities Committee from 2012–2014.

David E. Orin received his Ph.D. degree in Electrical Engineering from The Ohio State University in 1976. From 1976–1980, he taught at Case Western Reserve University. Since 1981, he has been at The Ohio State University, where he is currently a Professor Emeritus of Electrical and Computer Engineering. He was a sabbatical faculty at Sandia National Laboratories in 1996.

Orin's research interests center on humanoid walking and running, dynamic maneuvers in legged locomotion, and robot dynamics. He has over 150 publications. His research has been supported by NSF, Sandia National Laboratories, DARPA, NASA, NRL, Los Alamos National Laboratory, and the Honda Research Institute. He is a Fellow of the IEEE (1993). He was the President of the IEEE Robotics and Automation Society (2012–2013) and received the Distinguished Service Award from the Society in 2004. He serves as a Part Editor on the Editorial Board for the award-winning *Springer Handbook of Robotics*.